$$\phi^*_{47}=[-m_\ell m_d\bar{C}_{63}+m_\ell\bar{C}_{65}]\int(1/r)\,drdz \qquad \phi^*_{57}=[m_d\bar{C}_{43}-\bar{C}_{45}-m_\ell m_d\bar{C}_{63}+m_\ell\bar{C}_{65}]\int drdz$$

$$\phi^*_{67}=[-m_\ell m_d\bar{C}_{63}+m_\ell\bar{C}_{65}]\int(z/r)\,drdz \qquad \phi^*_{97}=[m_d\bar{C}_{63}-\bar{C}_{65}]\int drdz \qquad \phi^*_{38}=m_d\bar{C}_{43}\int rdrdz \qquad \phi^*_{48}=-m_\ell m_d\bar{C}_{63}\int drdz$$

$$\phi^*_{58}=[m_d\bar{C}_{43}-m_\ell m_d\bar{C}_{63}]\int rdrdz \qquad \phi^*_{68}=-m_\ell m_d\bar{C}_{63}\int zdrdz \qquad \phi^*_{98}=m_d\bar{C}_{63}\int rdrdz \qquad \phi^*_{19}=[\bar{C}_{36}-m_\ell\bar{C}_{56}]\int drdz$$

$$\phi^*_{29}=[\bar{C}_{16}+\bar{C}_{36}-m_\ell\bar{C}_{56}]\int rdrdz \qquad \phi^*_{39}=[\bar{C}_{36}+m_d\bar{C}_{43}-\bar{C}_{45}-m_\ell\bar{C}_{56}]\int zdrdz \qquad \phi^*_{49}=[-m_\ell m_d\bar{C}_{63}+m_\ell\bar{C}_{65}]\int(z/r)\,drdz$$

$$\phi^*_{59}=[m_d\bar{C}_{43}-\bar{C}_{45}-m_\ell m_d\bar{C}_{63}+m_\ell\bar{C}_{65}]\int zdrdz \qquad \phi^*_{69}=\bar{C}_{26}\int rdrdz+[-m_\ell m_d\bar{C}_{63}+m_\ell\bar{C}_{65}]\int(z^2/r)\,drdz$$

$$\phi^*_{79}=[m_\ell\bar{C}_{36}-\bar{C}_{56}]\int drdz \qquad \phi^*_{89}=m_\ell\bar{C}_{36}\int rdrdz \qquad \phi^*_{99}=[m_\ell\bar{C}_{36}-\bar{C}_{56}+m_d\bar{C}_{63}-\bar{C}_{65}]\int zdrdz \tag{3}$$

The compact elastic coefficients $\bar{C}_{ij}$ are defined in the Appendix of Ref. 1.

Thermal Load Vector

The changes to the thermal load vector for an anisotropic material are considerably simpler than the modifications to the stiffness matrix. Briefly, the thermal stress vector, which is used to compute the thermal loads, is derived from the product of the elasticity matrix and the thermal strain vector. The thermal stress in polar coordinates due to complete restraint of thermal expansion is

$$\sigma_{R\theta Z}=E_{R\theta Z}\alpha_{R\theta Z}\Delta t \tag{4}$$

where

$$\alpha_{R\theta Z}=\begin{Bmatrix}\tfrac{1}{2}(\alpha_X+\alpha_Y)+\tfrac{1}{2}(\alpha_X-\alpha_Y)\cos2\theta+\alpha_{XY}\sin2\theta\\ \alpha_Z\\ \tfrac{1}{2}(\alpha_X+\alpha_Y)+\tfrac{1}{2}(\alpha_Y-\alpha_X)\cos2\theta-\alpha_{XY}\sin2\theta\\ \alpha_{XZ}\cos\theta+\alpha_{ZY}\sin\theta\\ (\alpha_Y-\alpha_X)\sin2\theta\\ -\alpha_{XZ}\sin\theta+\alpha_{ZY}\cos\theta\end{Bmatrix} \tag{5}$$

III. Conclusions

This paper presents the modifications that must be made to the ASAAS finite-element code to enable the analysis of anisotropic materials fabricated into axisymmetric shapes and loaded axi- or asymmetrically. These modifications represent a significant increase in material modeling capability; i.e., any material that can be characterized by 21 elastic constants can be analyzed accurately. Furthermore, it enables one to analyze these solids-of-revolution with a pseudo-3-D computer code rather than having to resort to the more costly 3-D finite-element model.

Acknowledgments

This effort was supported in part by the Defense Nuclear Agency under its Hardened Reentry Vehicle Development Program (Contract DNA 001-75-C-0054) and by Prototype Development Associates, Santa Ana, Calif., under its IR and D program.

References

[1] Pardoen, G. C., Falco, A. D., and Crose, J. G., "Asymmetric Stress Analysis of Axisymmetric Solids with Rectangularly Orthotropic Properties," *AIAA Journal*, Vol. 14, Oct. 1976, pp. 1419-1426.

[2] Crose, J. G., "ASAAS, Asymmetric Stress Analysis of Axisymmetric Solids with Orthotropic Temperature Dependent Material Properties that Can Vary Circumferentially," Aerospace Corp., El Segundo, Calif., TR-0172 (S2816-15)-1, Dec. 29, 1971.

[3] Crose, J. G., "Stress Analysis of Axisymmetric Solids with Asymmetric Properties," *AIAA Journal*, Vol. 10, July 1972, pp. 886-871.

[4] Wilson, E. L., "Structural Analysis of Axisymmetric Solids," *AIAA Journal*, Vol. 3, Dec. 1965, pp. 2269-2274.

Blast Wave Analysis for Detonation Propulsion

Kibong Kim,* Giulio Varsi,† and Lloyd H. Back‡
Jet Propulsion Laboratory, Pasadena, Calif.

Introduction

A PROPULSION system based on chemical detonation rather than deflagration has been studied for the last several years (see, for example, Refs. 1-3). Larger specific impulse is obtainable from this system in high-density, high-pressure environments than from conventional rockets with propellant deflagration.

The performance of such a system was measured with the experimental system shown in Fig. 1, Ref. 1, in several different types of gases at different pressures. A conical nozzle (15.9 cm long) with a half angle, $\theta = 10$ deg, and a flat endwall (1.11 cm radius) was used. A small amount of explosive "detasheet" was placed flat against the nozzle endwall and detonated by a microdetonator. Results verify the advantages of the system over conventional rockets at high ambient pressures regardless of the type of gas.

A one-dimensional gasdynamic analysis of the system was carried out to explain qualitatively the general trend of the performance of the system at various conditions.[1] However, quantitative comparisons between this analysis and experiments were hindered by the inability to correctly calculate the blast wave coming out of the nozzle and the subsequent complex flow developing in and around the nozzle.

Two-Dimensional Computations

Reported herein is a two-dimensional inviscid calculation of this flowfield in the 69 bars, nitrogen environment. The Eulerian computer code DORF[4] was used with the explosive product gas assumed to follow the JWL equation of state. For details of computation, refer to Kim and Johnson.[3]

Figure 1 shows shock-front speed obtained from the local slope of the trajectory curves. Near the endwall, the shock speed could not be reliably determined because the shock was in the process of being formed and thus did not show a clear front. The experimentally obtained shock velocity[5] is compared in the figure as an asterisk.

Presented as Paper 76-401 at the AIAA 9th Fluid and Plasma Dynamics Conference, San Diego, Calif., July 14-16, 1976; submitted Aug. 16, 1976; revision received June 27, 1977.

Index categories: Jets, Wakes, and Viscid-Inviscid Flow Interactions; Shock Waves and Detonations; Electric and Advanced Space Propulsion.

*Resident Research Associate. Presently at the Naval Surface Weapons Center, White Oak Laboratory, Silver Spring, Md. Member AIAA.

†Group Supervisor. Member AIAA.

‡Member Technical Staff. Associate Fellow AIAA.

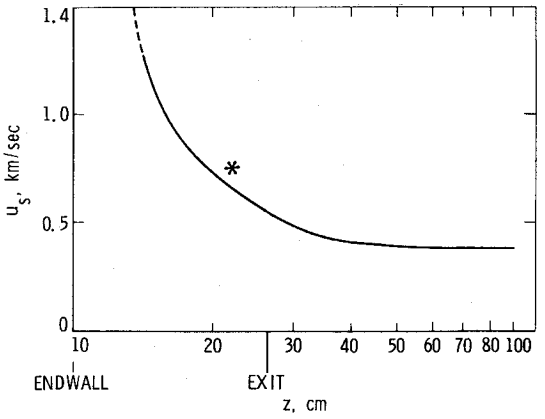

Fig. 1 Shock front velocity.

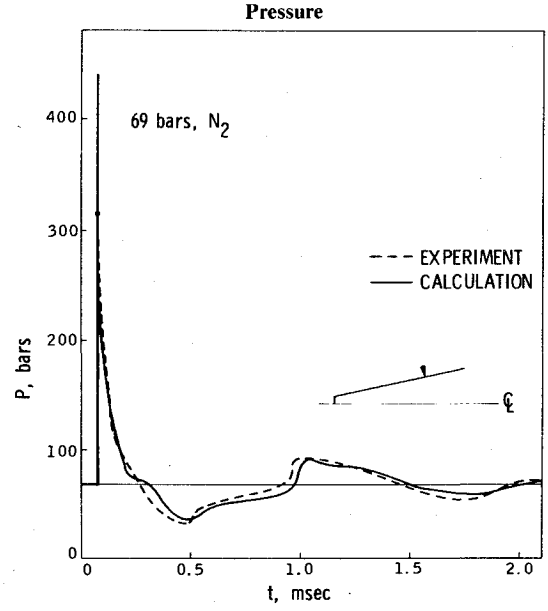

Fig. 2 Pressure-time history obtained at 11.5 cm from endwall.

Neglect of dissociation effects in the gas in the calculation was justified since the highest temperature obtainable in the present system was only about 1500 K behind the shock with the maximum speed of 1.5 km/sec.

Figure 2 shows the pressure profiles obtained by the pressure transducer located at 11.5 cm (axial distance) from the endwall (dashed line) and by the calculation (solid line) at the same location. The experimental curve was smoothed to eliminate noise. The peak pressure of the shock was much higher than the experimental value. This is associated with the artificially created pressure peak very near the nozzle wall that was caused by the fact that the 10-deg angle nozzle wall was inadequately simulated by rectangular blocks. This effect was more evident in the early times and became less significant later.

The calculated and measured slow decrease of pressure agree with each other, and a minimum value of -30 bars below ambient pressure is reached around 500 μsec after the detonation. This under-pressure is the reason for degradation of the specific impulse of the detonation-propulsion system. At approximately 500 μsec, a compression wave generated by the ambient gas moving into the nozzle reached the transducer location, as can be observed by the small step increase of pressure at this time. The pressure continued to increase gradually, as a result of more incoming compression waves from outside, until a reflected shock from the endwall once again passed this position moving outward, thus creating another pressure jump. Since the nozzle was being evacuated

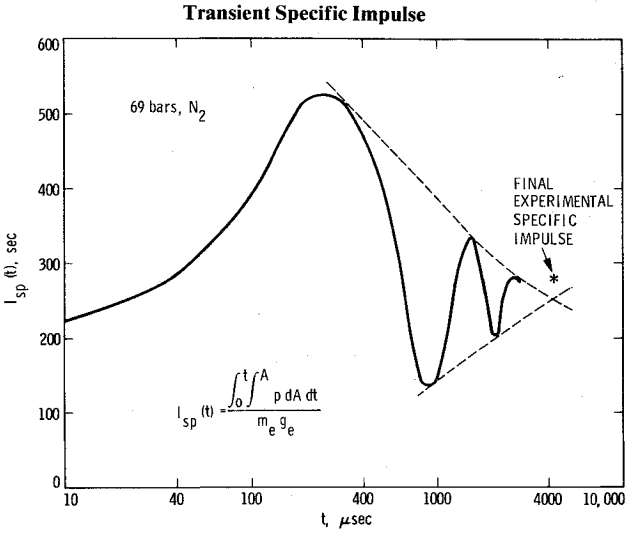

Fig. 3 Transient specific impulse.

behind this shock front, the pressure decreased to below the ambient pressure once again. This cycle was repeated until it finally settled down. The match between the experimental curve and the calculational curve in magnitude and frequency is remarkable.

The comparison of the specific impulse is shown in Fig. 3. The experimental value of the specific impulse was about 280 sec, whereas the extrapolation of the calculated transient specific impulse,

$$I_{sp}(t) = \frac{I}{m_e g_c} \int_0^t \int^A p\,dA\,dt$$

was around 250 sec. Here, p is the pressure acting on the wall; A, surface area; t, time; m_e, the mass of explosive; and g_c, the gravitational constant. This difference may come from the inadequate simulation of the nozzle wall by rectangular elements.

Compared to the one-dimensional numerical analysis,[1] the maximum transient-specific impulse was lower by about 50 sec (reaching 525 sec), but the final value was about 35 sec higher (final value of 250 sec). Also, the subsequent oscillation after the first main peak was much more pronounced in the two-dimensional calculation than the one-dimensional counterpart. This is because the ambient gas just outside the nozzle can play a more significant role without an imaginary barrier imposed as in the one-dimensional case. In other words, in the one-dimensional calculation when the nozzle is evacuated below the ambient pressure level, the only way for this partial vacuum to be recovered is for the outgoing gas to be slowed down enough further downstream to turn and flow back to the nozzle. The characteristic blast wave time in the one-dimensional calculation is several times larger than the characteristic time in the two-dimensional calculation, i.e., the time for a sound wave to propagate a nozzle length.[3] These peaks and valleys have not been clearly observed in the one-dimensional calculation since by the time the gas flows back to the nozzle, the strength of the waves became small.[1]

From Fig. 3, one can immediately recognize the effect of the under-pressure on the performance of the detonation propulsion system. After a maximum was reached, the transient-specific impulse dropped to a low of about 135 sec before oscillating back and forth and finally settling down at 250 sec. The initial drop by the under-pressure was about 390 sec and this was even larger in magnitude than the final specific impulse. This suggests that one might be able to improve the specific impulse, if one can fill the nozzle effectively when the nozzle is being evacuated.

In summary, the details of the blast wave resulting from the detonation-propulsion system is explained by both calculation and experiments. The relative importance of pressure peaks and valleys on the system performance is illustrated; especially, the importance of the under-pressure is emphasized.

Acknowledgment

This paper represents the results of one phase of research carried out at the Jet Propulsion Laboratory, California Institute of Technology, under Contract NAS 7-100, sponsored by the National Aeronautics and Space Administration.

References

[1]Kim, K., Back, L. H., and Varsi, G., "Measurements of Detonation Propulsion in Helium and Performance Calculations," *AIAA Journal*, Vol. 14, March 1976, pp. 310-312.

[2]Back, L. H. and Varsi, G., "Detonation Propulsion for High Pressure Environments," *AIAA Journal*, Vol. 12, Aug. 1974, pp. 1123-1130.

[3]Kim, K. and Johnson, W., "Exit of a Blast Wave from a Conical Nozzle," AIAA Paper 76-401, San Diego, Calif., June 1976.

[4]Johnson, W. E., "DORF 9 and RAD 9'-A Multi-Material Version with Strength of Materials and Radiation Diffusion," to be published by Computer Code Consultants.

[5]Varsi, G., Back, L. H., and Kim, K., "Blast Wave in a Nozzle for Propulsion Applications," *Acta Astronautica*, Vol. 3, 1976, pp. 141-156.

Stability of a Future Generation Spacecraft Attitude Control System

A. S. C. Sinha*
Purdue University, Indianapolis, Ind.
and
A. Nadkarni†
Old Dominion University, Va.

I. Introduction

THE system under consideration at NASA Langley Research Lab., represents a new concept in attitude control of spacecraft. It will provide a better attitude control, more payload capacity in the spacecraft, and hopefully will meet increasing demands in satellite communication, weather prediction, etc., which need more payload, and unbalanced loading. An accurate modeling of internal energy dissipation is extremely difficult. However, the energy dissipation in either the high-speed Annular Momentum Control Device (AMCD) or the despun main spacecraft structure introduced through a damping mechanism, is modeled by one ball-in-the-tube damper with one degree of freedom.

The subscript of a representation of a vector in a three-dimensional space denotes that vector in a particular coordinate system. For example, (T_{ax}, T_{ay}, T_{az}) and (T_{sx}, T_{sy}, T_{sz}) are the vector representations of bearing interaction torques T_a and T_s in (x,y,z), respectively, where subscript a denotes AMCD and s denotes spacecraft. The projections of a vector T_a in x, y, and z coordinates are denoted by T_{ax}, T_{ay}, and T_{az}. G_{ax}, G_{ay}, G_{az} and G_{sx}, G_{sy}, G_{sz} are external disturbance torques for the AMCD rim and spacecraft due to three balancing masses and one ball-in-tube damper. The vectors ω_a, I_a and ω_s, I_s are angular velocity and transverse moment of inertia of the a coordinate system and the s system, respectively. H_a and H_s are total angular momentum of AMCD and spacecraft, respectively. The Euler angles chosen to represent the positions of the a and s coordinate axes with respect to an inertial axis set are ϕ and θ. α and β are spacecraft rotation angle and rim rotation angle, respectively. P and P' represent damper motion along the z axis. The reader is strongly encouraged to see Ref. 1 for details of the notations and development of equations of motion for dissipative AMCD spacecraft.

Received Dec. 23, 1976; revision received July 1, 1977.
Index categories: Aerodynamics; Guidance and Control.

*Associate Professor, Department of Electrical Engineering, School of Engineering and Technology.
†Research Assistant, Department of Aerospace.

II. Stability Criteria

The analysis is based on the dissipative dual-spin configuration. The AMCD spacecraft is comprised of three parts: 1) the primary part of the spacecraft, assumed to be essentially the right circular cylinder; 2) the AMCD spin assembly configuration consists of a rotating rim (no central hub) suspended by noncontacting magnetic bearings and powered by a noncontacting linear electromagnetic motor (see Ref. 2); 3) the energy dissipation in either the high-speed AMCD or the despun main spacecraft structure, introduced through a damping mechanism, is modeled by one ball-in-tube damper. Three particles, each of whose mass is equal to the total mass of the damping mechanism, are rigidly attached to the spacecraft in such a way that the combination damper and three particles become inertially symmetrical about the spin axis.

The equation of motion for the dissipative AMCD-spacecraft can be written as

$$I_a\ddot{\phi}_a + K_\phi(\phi_a - \phi_s) + K_{\dot\phi}(\dot\phi_a - \dot\phi_s) + H_a\dot\theta_a + K_{\dot\phi}\dot\beta(\theta_a - \theta_s) - G_{ax} = 0 \tag{1}$$

$$I_a\ddot{\theta}_a + K_\phi(\theta_a - \theta_s) + K_{\dot\phi}(\dot\theta_a - \dot\theta_s) + H_a\dot\phi_a - K_{\dot\phi}\dot\beta(\phi_a - \phi_s) - G_{ay} = 0 \tag{2}$$

$$I_s\ddot{\phi}_s - K_\phi(\phi_a - \phi_s) - K_{\dot\phi}(\dot\phi_a - \dot\phi_s) + H_s\dot\theta_s - K_{\dot\phi}\dot\beta(\theta_a - \theta_s) - G_{sx} = 0 \tag{3}$$

$$I_s\ddot{\theta}_s - K_\phi(\theta_a - \theta_s) - K_{\dot\phi}(\dot\theta_a - \dot\theta_s) - H_s\dot\phi_s + K_{\dot\phi}\dot\beta(\phi_a - \phi_s) - G_{sy} = 0 \tag{4}$$

$$\dot{H}_a = G_{az} = I_{az}\ddot{\alpha} \tag{5}$$

$$H_s = G_{sz} = I_{az}\ddot{\beta} \tag{6}$$

$$c\dot{P} + kP + m[\ddot{P} - \dot\omega_y a + \omega_z\omega_x a - P(\omega_x^2 + \omega_y^2)] = 0 \tag{7}$$

$$c\dot{P}' + k'P' + m'[\ddot{P}' - \dot\omega_y' a' + \omega_z'\omega_x' a' - P'(\omega_x'^2 + \omega_y'^2)] = 0 \tag{8}$$

where

$$G_{az} = (-ma\sin\alpha)\ddot{P};\quad G_{ay} = (ma\cos\alpha)\ddot{P} \tag{9}$$

$$G_{sx} = (-m'a'\sin\beta)\ddot{P}';\quad G_{sy} = (m'a'\cos\beta)\ddot{P}' \tag{10}$$

are linearized disturbance torques. The detailed derivation of equations from the first principle are reported in Ref. 1, and are omitted here for the sake of brevity. The stability of the origin is examined. The linearized equation of motion about the equilibrium point gives the following differential equation of motion:

$$\hat{M}(t)\ddot{x}(t) + \hat{B}(t)\dot{x}(t) + \hat{K}(t)x(t) = 0 \tag{11}$$